Nanostructures and Capacitive Characteristics of Hydrous Manganese Oxide Prepared by Electrochemical Deposition

Chi-Chang Hu*,z and Chen-Ching Wang

Department of Chemical Engineering, National Chung Cheng University, Chia-Yi 621, Taiwan

Amorphous manganese oxide deposits with nanostructures (denoted as a-MnO$_x$·nH$_2$O) were electrochemically deposited onto graphite substrates from 0.16 M MnSO$_4$·5H$_2$O with pH 5.6 by means of the potentiostatic, galvanostatic, and potentiodynamic techniques. The maximum specific capacitance of a-MnO$_x$·nH$_2$O deposits plated in different modes, measured from cyclic voltammetry at 25 mV s^{-1}, is about 230 F g^{-1} in a potential window of 1.0 V. The high electrochemical reversibility, high-power characteristics, good stability, and improved frequency responses in 0.1 M Na$_2$SO$_4$ for these nanostructured a-MnO$_x$·nH$_2$O deposits prepared by electrochemical methods demonstrate their promising potential in the application to electrochemical supercapacitors. The nanostructure of a-MnO$_x$·nH$_2$O, clearly observed by means of a scanning electron microscope, was found to depend strongly on the deposition mode. The similar capacitive performance of all deposits prepared in different modes was attributable to their nonstoichiometric nature with a very similar oxidation state, demonstrated by XPS spectra.

© 2003 The Electrochemical Society. [DOI: 10.1149/1.1587725] All rights reserved.

Batteries and capacitors are usually the electrical energy storage devices in many applications. The energy density of the former devices is usually much higher than that of the latter while the power density of the latter devices is several orders of magnitude higher than most primary energy storage units. Since the demand for power sources delivering significant energy in the high-power or pulse-power form has increased, the development of capacitors with high energy densities (*i.e.*, supercapacitors) for these applications has been an interesting subject of much research.[1-3] Moreover, it is now reasonable to separate the power and energy delivering devices in an integrated power system to enhance their respective performance. This point of view is supported by the fact that supercapacitors have been found to significantly improve the service life of some primary energy storage units,[3,4] further attracting the attention of many researchers.[5-8]

The energies stored in supercapacitors mainly come from either the electrical double-layer (dl) capacitance of the materials with high specific surface areas[1-3,5] or the faradaic pseudocapacitance of electroactive materials with several oxidation states.[6-8] The former devices are also called dl capacitors, usually consisting of highly porous carbon material.[1-3,5,9] The latter devices are also called capteries or pseudocapacitors since the mechanism of energy storage within the electroactive materials is very similar to that of rechargeable batteries.[1,2,6-8,10]

Due to cost considerations, cheaper candidates with good capacitive characteristics have attracted much attention. Since pseudocapacitance comes mainly from the reversible redox transitions of the electroactive materials, transition-metal oxides (*e.g.*, oxides of Ru, Mn, Mo, V, Cr, W, Re, Ni, Co, etc.) and conducting polymers with several oxidation states or structures are considered to be promising materials applicable in supercapacitors.[1,2,6-8,10-12] Recently, hydrous manganese oxides prepared by the sol-gel-derived, chemical coprecipitation, or cyclic voltammetric methods were found to possess capacitive-like characteristics[13-15] although the electrochemical reversibility of the redox transitions within manganese-oxide-based electrodes, suitable for rechargeable batteries,[16] is usually too low to be applicable for supercapacitors. However, the capacity of a very thin MnO$_2$ film (1-4 μg cm^{-2}) prepared by the sol-gel-derived method is unacceptable although its specific capacitance is very high (*ca.* 700 F g^{-1}).[13] Moreover, pure a-MnO$_2$·nH$_2$O prepared by a chemical coprecipitation method was found to possess poor capacitive characteristics due to the high resistance of bulk a-MnO$_2$·nH$_2$O.[14] Based on the above points of view, anodic deposition was successfully developed to prepare an amorphous and non-

stoichiometric manganese oxide (denoted as a-MnO$_x$·nH$_2$O) with excellent capacitive characteristics (*i.e.*, high reversibility, high pulse power density, acceptable capacity, and good stability).[17,18] Thus, a-MnO$_x$·nH$_2$O prepared by anodic deposition is expected to be one of the most promising potential candidates in the application to supercapacitors.

In our previous study, the capacitive behavior as well as the structure of a-MnO$_x$·nH$_2$O films was probably affected by the deposition variables and the deposition modes.[17,18] The purpose of this work is to show how the electrochemical deposition mode influences the nanostructure of a-MnO$_x$·nH$_2$O deposits. The ideally capacitive performance of this hydrous oxide with an acceptable capacity in the potential window of *ca.* 1.0 V is also discussed.

Experimental

The a-MnO$_x$·nH$_2$O deposits were electroplated directly onto 10 × 10 × 3 mm graphite substrates (Nippon Carbon EG-NPL, N.C.K., Japan). These substrates were first abraded with ultrafine SiC paper, degreased with acetone and water, then etched in a 0.1 M HCl solution at room temperature (*ca.* 26°C) for 10 min, and finally degreased with water in an ultrasonic bath. The exposed geometric area of these pretreated graphite supports is 1 cm^2 while the other surface areas were insulated with polytetrafluoroethylene (PTFE) coatings. The plating solutions, consisting of 0.16 M MnSO$_4$·5H$_2$O with pH of 5.6, were stirred on a hot plate during the deposition process. The deposition was performed by the potentiostatic method at 0.8 V (denoted as a-MnO$_x$·nH$_2$O-P), the galvanostatic mode at 3.7 mA cm^{-2} (a-MnO$_x$·nH$_2$O-G) with a total passed charge of 0.3 C cm^{-2}, or cyclic voltammetry (CV) at 10 mV s^{-1} between 0.4 and 1.0 V for 30 cycles (a-MnO$_x$·nH$_2$O-CV). After deposition, the PTFE films were removed from the electrodes. These electrodes were first rinsed with a flow of pure water for *ca.* 30 s and then dipped into a beaker containing pure water (at room temperature) that was stirred by a hot plate for 5 min. After cleaning, these electrodes were dried in a vacuum oven at room temperature overnight.

The oxide loading of hydrous oxide-coated electrode is the weight difference of the electrode without PTFE coating before and after the application of oxide deposition as obtained with a microbalance with an accuracy of 10 μg (Sartorius BP 211D, Germany). The average loading for the a-MnO$_x$·nH$_2$O-P, a-MnO$_x$·nH$_2$O-CV, and a-MnO$_x$·nH$_2$O-G was 0.24, 0.22, and 0.17 mg cm^{-2}, respectively. The X-ray diffraction (XRD) patterns obtained from XRD analysis (Rigaku X-ray diffractometer using a Cu target) at an angle speed of 4° (2θ) min^{-1} show that all oxide deposits prepared with the different electrochemical modes are amorphous (not shown here). Surface morphologies of these oxide depos-
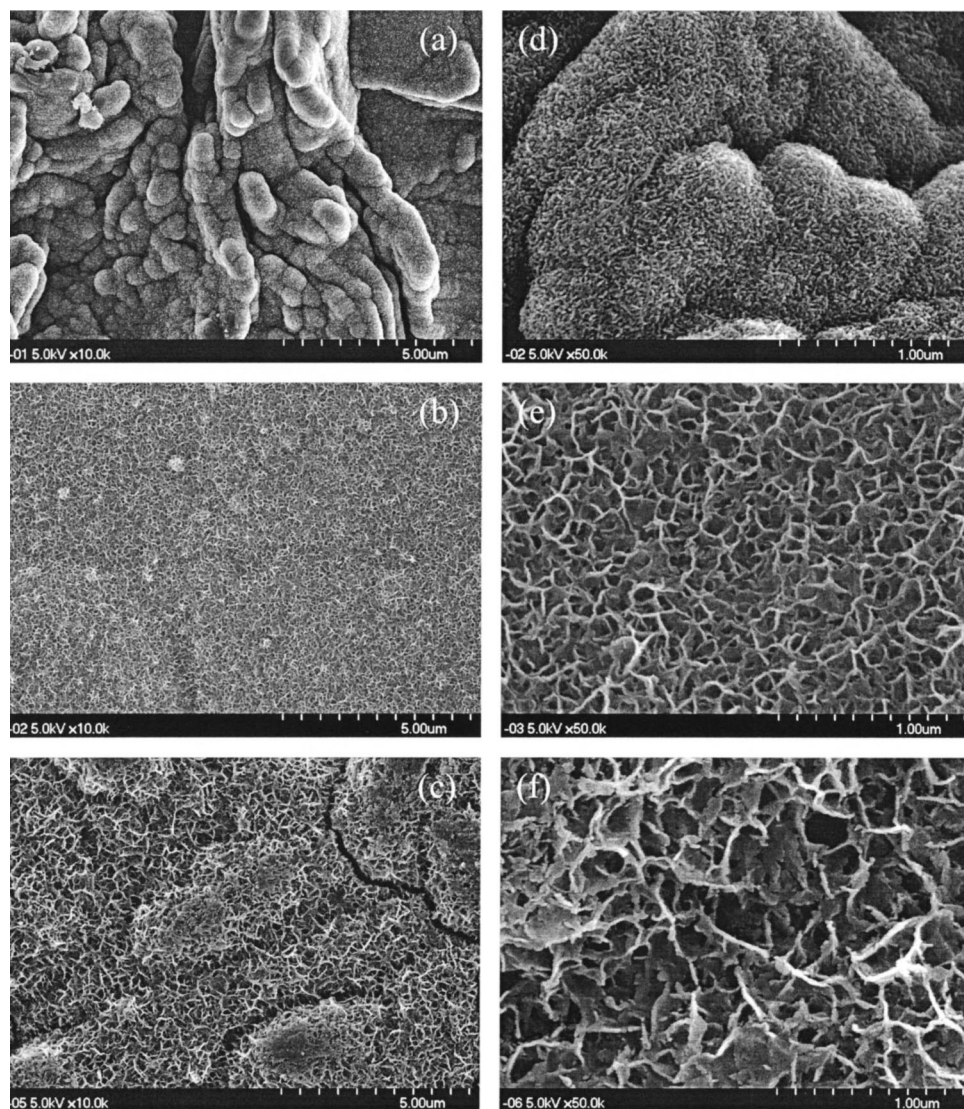
Figure 1. SEM photographs of (a,d) a-MnO$_x$·nH$_2$O-P, (b,e) a-MnO$_x$·nH$_2$O-CV, and (c,f) a-MnO$_x$·nH$_2$O-G.

its were examined by a scanning electron microscope (SEM, Hitachi S-3500, Japan). X-ray photoelectron spectroscopic (XPS) measurements were performed with an ESCA 210 (VG Scientific Ltd.) spectrometer. XPS spectra employed Mg Kα ($h\nu$ = 1253.6 eV) irradiation as the photosource, with a primary voltage of 12 kV and an emission current 17 mA. The analysis chamber pressure during scans was approximately 10^{-10} mbar.

Electrochemical measurements for a-MnO$_x$·nH$_2$O deposits were performed by means of electrochemical analyzer systems, CHI 633A (CH Instruments, USA). The impedance spectrum analyzer, IM6 (ZAHNER, Germany), with Thales software, was employed to measure and analyze the ac impedance spectra. The potential amplitude of the ac was equal to 10 mV while the frequency range was from 100 mHz to 30 kHz. All experiments were carried out in a three-compartment cell. An Ag/AgCl electrode (Argenthal, 3 M KCl, 0.207 V *vs.* saturated hydrogen electrode at 25°C) was used as the reference and a piece of platinum gauze with an exposed area equal to 4 cm^2 was employed as the counter electrode. A Luggin capillary, whose tip was about 2 mm from the surface of the working electrode during voltammetric measurements, was used to minimize errors due to iR drop in the electrolyte.

All solutions used in this work were prepared with 18 MΩ cm water produced by a reagent water system (MILLI-Q SP, Japan), and all reagents not otherwise specified in this work were Merck, GR. In

addition, the electrolytes containing 0.1 M Na$_2$SO$_4$, used to study the capacitive behavior of a-MnO$_x$·nH$_2$O, were degassed with purified nitrogen gas before measurements, and a nitrogen blanket was used during the measurements. The solution temperature was maintained at 25°C by means of a water thermostat (HAAKE DC3 and K20).

Results and Discussion

Nanostructures of a-MnO$_x$·nH$_2$O.—Typical SEM photographs for a-MnO$_x$·nH$_2$O-P, a-MnO$_x$·nH$_2$O-CV, and a-MnO$_x$·nH$_2$O-G deposits are shown in Fig. 1a, d, b, e, and c, f, respectively. In Fig. 1a, the morphology of a-MnO$_x$·nH$_2$O-P is relatively rough, consisting of many large spherical grains under lower SEM amplification. However, under higher magnification of 50,000 times, these large grains are found to be composed of many short MnO$_x$ rods with a mean diam of *ca.* 15 nm (see Fig. 1d). Moreover, these rods are entangled with each other to form the relatively compact spherical grains. In Fig. 1b, a-MnO$_x$·nH$_2$O-CV is highly porous and uniform. The morphology of this deposit clearly shows a nanostructure in a three-dimensional (3-D) network. In addition, no obvious grain boundaries can be found on this deposit. In Fig. 1e, the mean diameter of these MnO$_x$ nanowires is about 20 nm and the average diameter of the mesopores is about 100 nm. Moreover, sev-
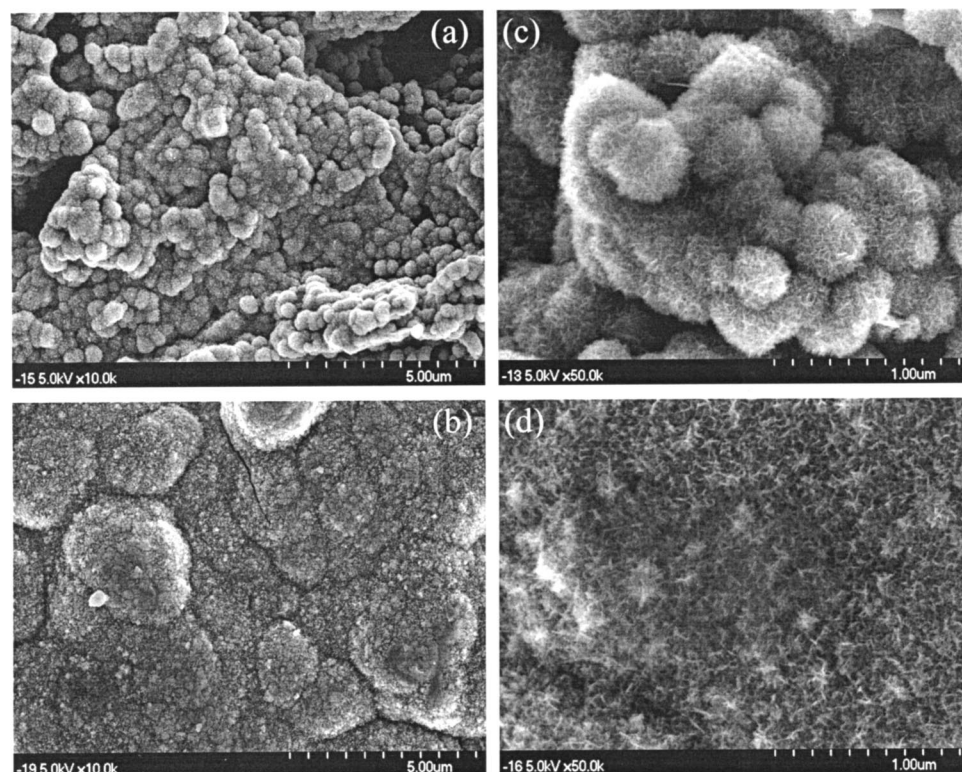
Figure 2. SEM photographs of a-MnO$_x$·nH$_2$O-CV with (a,c) 5 and (b,d) 10 cycles of CV deposition between 0.4 and 1.0 V.

eral mesopores are filled with MnO$_x$ films. In Fig. 1c, the morphology of a-MnO$_x$·nH$_2$O-G is very similar to that of a-MnO$_x$·nH$_2$O-CV while a grain-like morphology under lower SEM magnification is found for the former deposit. Under higher magnification of 50,000 times in Fig. 1f, a nanostructured morphology in a 3-D network is also clearly found while the mean diam of the MnO$_x$ nanowires is *ca.* 30 nm and the mesopores of this deposit are much larger than those on MnO$_x$·nH$_2$O-CV. A comparison of Fig. 1a-f reveals two facts. First, the morphology of a-MnO$_x$·nH$_2$O is strongly dependent upon the deposition mode, which should significantly influence the utilization of MnO$_x$ during electrochemical energy storage. Second, through electrochemical deposition, nanostructured MnO$_x$ materials can be prepared easily.

In order to gain more information about the 3-D nanostructured a-MnO$_x$·nH$_2$O film, the morphology of a-MnO$_x$·nH$_2$O-CV with 5 and 10 cycles of CV deposition are shown as Fig. 2a, c and 2b, d, respectively. In Fig. 2a, the rough surface of this a-MnO$_x$·nH$_2$O-CV electrode is due to the macrorough nature of graphite substrates that are completely covered with many spherical oxide grains under lower SEM amplification. These spherical oxide grains, under higher magnification of 50,000 times, are composed of hundreds of a-MnO$_x$·nH$_2$O nanowires (see Fig. 2c). On the other hand, when 10 cycles of CV deposition are applied, these grains are merged into larger grains while their grain boundaries become relatively unclear (Fig. 2b). Moreover, the diameter and length of the a-MnO$_x$·nH$_2$O nanowires become larger and longer with increasing numbers of deposition cycles (Fig. 2d). Based on the above results and discussion, a-MnO$_x$·nH$_2$O nanowires should be easily formed by the CV deposition technique.

In order to gain constructive information about a-MnO$_x$·nH$_2$O prepared with different deposition modes, the binding energy of the oxymanganese species was examined in this work. Typical XPS spectra of Mn 2p$_{3/2,1/2}$, and O 1s for various a-MnO$_x$·nH$_2$O deposits prepared by different modes are shown in Fig. 3. The broad peak of Mn 2p$_{3/2}$ in Fig. 3a-c is located around 642.0 eV, indicating that the mean oxidation state of Mn is not significantly affected by

changing the deposition modes. In addition, the difference of peak separation between Mn 2p$_{3/2}$ and 2p$_{1/2}$ is about 11.5 eV for all spectra, further supporting the above statement since the binding energy difference of Mn 2p$_{3/2}$ and 2p$_{1/2}$ can be used to indicate the oxidation state of Mn.[19] On the other hand, the broad peaks of Mn 2p$_{3/2}$ and 2p$_{1/2}$ in these spectra indicate that a-MnO$_x$·nH$_2$O is a
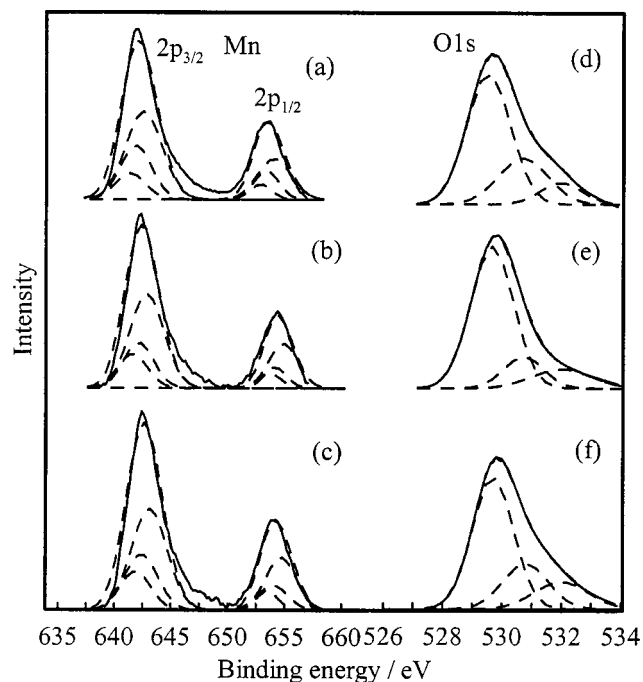
Figure 3. XPS spectra in (a-c) Mn 2p$_{3/2,1/2}$, (d-f) O 1s region for (a,d), a-MnO$_x$·nH$_2$O-P, (b,e), a-MnO$_x$·nH$_2$O-CV, and (c,f) a-MnO$_x$·nH$_2$O-G.

Table I. The relative amount of Mn(II), Mn(III), and Mn(IV) as well as Mn-O-Mn, Mn-O-H, and H-O-H within a-MnO$_x$·nH$_2$O-P, a-MnO$_x$·nH$_2$O-CV, and a-MnO$_x$·nH$_2$O-G.

		Mn 2p			O 1s		
		Mn(II)	Mn(III)	Mn(IV)	Mn-O-Mn	Mn-O-H	H-O-H
a-MnO$_x$·nH$_2$O-P	(2p$_{3/2}$)	13.86	29.69	56.45	64.21	25.68	10.11
	(2p$_{1/2}$)	13.91	29.46	56.63			
a-MnO$_x$·nH$_2$O-CV	(2p$_{3/2}$)	17.98	24.30	57.72	71.74	14.82	13.44
	(2p$_{1/2}$)	16.29	23.34	60.37			
a-MnO$_x$·nH$_2$O-G	(2p$_{3/2}$)	16.89	27.90	55.21	60.34	23.07	16.59
	(2p$_{1/2}$)	15.18	26.86	57.96			

mixture consisting of oxy-/hydroxyl-manganese species in various oxidation states. Accordingly, Mn 2p$_{3/2}$ and 2p$_{1/2}$ spectra are decomposed into three pairs of constituents (*i.e.*, for Mn 2p$_{3/2}$ 641.7, 642.4, and 642.9 eV, respectively). The above result reveals that all a-MnO$_x$·nH$_2$O deposits electroplated by different modes can be considered as an oxide aggregation consisting of Mn(II), Mn(III), and Mn(IV) species. From a comparison of Fig. 3d-f, the main peak of O 1s is located around 529.8 eV, which is approximately independent of the deposition mode. However, the relative amount of Mn-O-Mn, Mn-O-H, and H-O-H is a function of deposition modes when the O 1s spectrum is decomposed into three constituents (*i.e.*, 529.7, 530.9, and 531.8 eV, respectively).[20,21] Based on the relative area of the constituent peaks for Mn 2p$_{3/2}$, 2p$_{1/2}$, and O 1s spectra, data corresponding to the relative amount of Mn(II), Mn(III), and Mn(IV) as well as that of Mn-O-Mn, Mn-O-H, and H-O-H are shown in Table I. Note that the relative amounts of Mn(II), Mn(III), and Mn(IV) calculated from Mn 2p$_{3/2}$ and 2p$_{1/2}$ are approximately equal, indicating the good fitting of these XPS spectra. Based on the data shown in Table I, the mean oxidation of Mn in a-MnO$_x$·nH$_2$O-P, a-MnO$_x$·nH$_2$O-CV, and a-MnO$_x$·nH$_2$O-G is 3.43, 3.40, and 3.38, respectively. Accordingly, all a-MnO$_x$·nH$_2$O deposits prepared in this work are undoubtedly of a nonstoichiometric structure. In addition, this nonstoichiometric nature is believed to be responsible for the amorphous structure of a-MnO$_x$·nH$_2$O plated with different electrochemical modes. Based on the relative area of the three constituents for O 1s, anhydrous Mn oxide (*i.e.*, Mn-O-Mn) should be the main species in a-MnO$_x$·nH$_2$O. However, a significant amount of Mn-O-H and water species can be found in these a-MnO$_x$·nH$_2$O deposits, revealing their hydrous nature. From the above results and discussion, a-MnO$_x$·nH$_2$O deposits plated with different modes possess a nonstoichiometric structure with a hydrous characteristic. Moreover, the mean oxidation state of Mn is not significantly affected by changing the deposition methods.

Capacitive characteristics of a-MnO$_x$·nH$_2$O.—Typical CV diagrams of a-MnO$_x$·nH$_2$O-P, a-MnO$_x$·nH$_2$O-CV, and a-MnO$_x$·nH$_2$O-G deposits measured in 0.1 M Na$_2$SO$_4$ at 50 mV s^{-1} are shown in Fig. 4 as curves 1-3, respectively. Note that there are no obvious redox peaks between *ca.* 0.15 and 0.85 V on curves 1-3 and the large background currents on these curves are not attributable to the dl responses. These results reveal the ideality of capacitive performance for a-MnO$_x$·nH$_2$O deposits plated by electrochemical methods. Moreover, all curves show a rectangular-like and symmetric voltammogram at a high scan rate, demonstrating the high power property of this electrode material. On the other hand, a gradual increase in voltammetric currents commencing at *ca.* 0.85 V on the positive sweep of these curves and an poorly defined reduction peak found at *ca.* 0.9 V on the following negative sweep indicate the presence of a redox pair in this potential region. This redox couple probably catalyzes the oxygen evolution reaction (OER) since this reaction has been found to be catalyzed by several redox couples with suitable redox potentials.[22] Hence, the upper limit of the operational potential window for a supercapacitor employing a-MnO$_x$·nH$_2$O as the electrode material should be ≤1.0 V. The

gradual increase in cathodic currents occurring at *ca.* 0.15 V on the negative sweep of curves 1–3 and the presence of an barely detectible anodic peak at *ca.* 0.12 V on the corresponding positive sweep also suggest the presence of a relatively irreversible redox couple. Thus, the lower limit of operational potential window for this electrode material in supercapacitors should be positive of 0 V. Based on the above results and discussion, the suitable potential window for the operation of an a-MnO$_x$·nH$_2$O supercapacitor in Na$_2$SO$_4$ should be between 0 and 1.0 V.

Due to the high power demand in supercapacitors[1,2,17,18] and the fact that the power property of an electrode material is strongly dependent upon the electrochemical kinetics of redox transitions,[1,2,7,10,11] the power property of various a-MnO$_x$·nH$_2$O deposits prepared by different electroplating modes is examined by changing the scan rate of CV. Note that for an ideal capacitor, the dependence of capacitive currents, i, on scan rates, v, of CV obeys the following equation where C is the capacitance[23]

$$i = C \times v \qquad [1]$$

Accordingly, voltammetric currents must be directly proportional to the applied scan rate. Hence, Eq. 1 can be used to examine the high power property of potential materials for supercapacitors, based on the deviation of current from linearity at a specified scan rate. Typical results of capacitive currents against the scan rate of CV for a-MnO$_x$·nH$_2$O-P, a-MnO$_x$·nH$_2$O-CV, and a-MnO$_x$·nH$_2$O-G deposits measured in 0.1 M Na$_2$SO$_4$ are shown in Fig. 5. Note the linear dependence of voltammetric currents on the scan rate from 5 to 50 mV s^{-1}, revealing the high power property of all
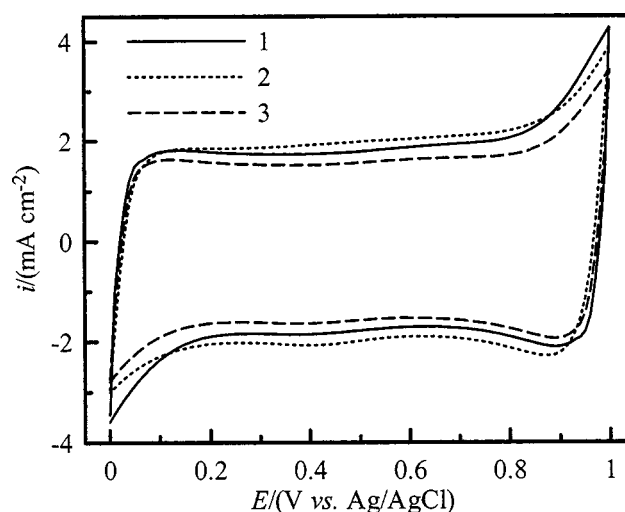
Figure 4. Cyclic voltammograms of (1) a-MnO$_x$·nH$_2$O-P, (2) a-MnO$_x$·nH$_2$O-CV, and (3) a-MnO$_x$·nH$_2$O-G measured in 0.1 M Na$_2$SO$_4$ at 50 mV s^{-1}.
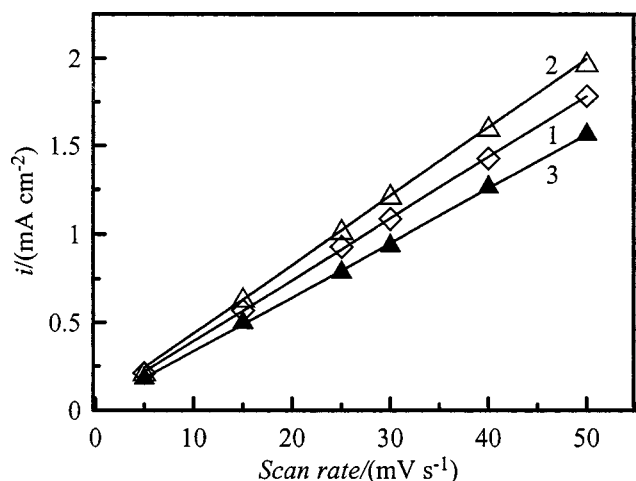
Figure 5. Current (i) *vs.* scan rate (v) plots, where i values were obtained at 0.5 V from CVs for (1) a-MnO$_x$·nH$_2$O-P, (2) a-MnO$_x$·nH$_2$O-CV, and (3) a-MnO$_x$·nH$_2$O-G in 0.1 M Na$_2$SO$_4$.

Figure 7. A Nyquist impedance spectrum of a-MnO$_x$·nH$_2$O-CV measured at the OCP ($\approx$320 mV *vs.* Ag/AgCl) in 0.1 M Na$_2$SO$_4$.

a-MnO$_x$·nH$_2$O deposits in Na$_2$SO$_4$ (*e.g.*, the specific power of a-MnO$_x$·nH$_2$O-G can reach 12 kW/kg). In addition, the capacitance deduced from the slope of lines 1-3 is *ca.* 35.1, 39.3, and 31.4 mF cm^{-2} for a-MnO$_x$·nH$_2$O-P, a-MnO$_x$·nH$_2$O-CV, and a-MnO$_x$·nH$_2$O-G deposits, respectively, which depends on the oxide loading. Moreover, the above capacitance values are smaller than those deduced from the voltammetric charges integrated from their CV curves measured at 25 mV s^{-1} (*i.e.*, 38.6, 42.7, and 38.4, mF cm^{-2}, respectively), probably due to the contribution of the redox currents at potentials negative of 0.1 V or more positive than 0.9 V. On the other hand, the large pseudocapacitance and high power characteristics do indicate that a-MnO$_x$·nH$_2$O deposits plated with different electrochemical modes are potential candidates for the application to electrochemical supercapacitors. In addition, their capacitance is approximately constant over a relatively wide potential region (*i.e.*, from *ca.* 0.1 to 0.9 V), revealing the ideally capacitive responses of this material in the test electrolyte.

The stability of various a-MnO$_x$·nH$_2$O deposits plated by different modes was also examined in this work by the application of repeated potential cycling in Na$_2$SO$_4$. Typical results of a-MnO$_x$·nH$_2$O-P, a-MnO$_x$·nH$_2$O-CV, and a-MnO$_x$·nH$_2$O-G are

Figure 6. Specific capacitance decay for (1) a-MnO$_x$·nH$_2$O-G, (2) a-MnO$_x$·nH$_2$O-CV, and (3) a-MnO$_x$·nH$_2$O-P in 0.1 M Na$_2$SO$_4$ against the cycle number of CV in the stability tests. Cyclic voltammograms were measured at 25 mV s^{-1} in 0.1 M Na$_2$SO$_4$.
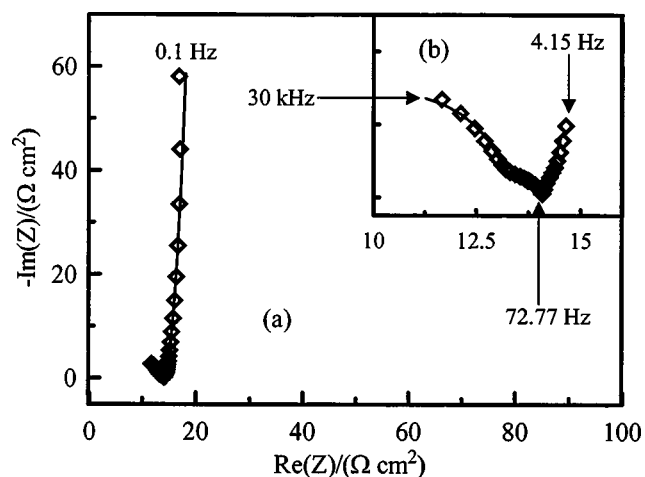
shown in Fig. 6. Note that the specific capacitance of all deposits gradually decreased to about 95% of the original value after 100 cycles of the CV test while a very slow degradation rate is found in the following 400 cycles. The total loss in specific capacitance for a-MnO$_x$·nH$_2$O-P, a-MnO$_x$·nH$_2$O-CV, and a-MnO$_x$·nH$_2$O-G deposits was 7.6, 5.8, and 7.5%, respectively, after the 500 cycle CV test. The low loss in specific capacitance of these a-MnO$_x$·nH$_2$O deposits demonstrates their good stability in Na$_2$SO$_4$ and their promising potential in the application to electrochemical supercapacitors.

Recently, many efforts have focused on increasing the power density and improving the frequency response of potential electrode materials for supercapacitors.[24,25] The key factor influencing the power and frequency performance of an electrochemical supercapacitor is the equivalent series resistance (ESR) that is mainly determined by the charge-transfer resistance of the redox reactions (especially for electroactive materials), the electronic conductivity of electrode materials and the ionic conductivity of electrolytes. In addition, the frequency responses of an electrode material can be clearly characterized by investigating the electrochemical impedance spectra (EIS) through means of the equivalent circuit model. A typical Nyquist impedance spectrum, measured at the open-circuit potential (OCP, $\approx$320 mV *vs.* Ag/AgCl) in 0.1 M Na$_2$SO$_4$, for a-MnO$_x$·nH$_2$O-CV is shown in Fig. 7.

In Fig. 7, an impedance arc of a one-fourth circle is visible in the high frequency region; meanwhile a small arc is merged into this semicircle in the middle-frequency region for this EIS spectrum. This small impedance arc is also visible for a-MnO$_x$·nH$_2$O-G while it is absent for the a-MnO$_x$·nH$_2$O-P deposit. This small arc may be attributable to the mesoporous and 3-D network nanostructures of the former two a-MnO$_x$·nH$_2$O deposits, which also increase the utilization of Mn oxide. The high frequency arc is attributable to the dl process since the response of this process should be much faster than that of a faradaic reaction. In the low frequency region (*ca.* <70 Hz), an approximately vertical increase in impedance on the imaginary part is visible with decreasing the ac frequency. This result demonstrates that the low frequency impedance responses show typical capacitive characteristics, which should be mainly governed by a faradaic process of the electroactive material. In addition, the capacitive responses in the low frequency region reveal the capacitive-like characteristics of the redox transitions within a-MnO$_x$·nH$_2$O. Note that the onset frequencies where a-MnO$_x$·nH$_2$O-P, a-MnO$_x$·nH$_2$O-CV, and a-MnO$_x$·nH$_2$O-G begin to behave as a capacitor are equal to *ca.* 41, 72, and 46 Hz, respectively, which are much higher than that of an electrode material consisting of porous carbon and carbon nanotubes.[24,25] This im-

proved frequency response of a-MnO$_x \cdot n$H$_2$O may be linked to their nanostructures, favoring ion exchange during the redox transitions. From the above results and discussion, supercapacitors composed of a-MnO$_x \cdot n$H$_2$O should have an improved frequency response and a high power property, consistent with the voltammetric results.

From all the above results and discussion, nanostructured a-MnO$_x \cdot n$H$_2$O deposits fabricated by electrochemical deposition from MnSO$_4 \cdot 5$H$_2$O with pH of 5.6 exhibit ideally capacitive behavior in Na$_2$SO$_4$ for the application to electrochemical supercapacitors.

Conclusions

Nanostructured and amorphous MnO$_x \cdot n$H$_2$O deposits, fabricated by potentiostatic, galvanostatic, and potentiodynamic techniques from 0.16 M MnSO$_4 \cdot 5$H$_2$O with an initial pH value of 5.6, showed ideally capacitive characteristics (*i.e.*, large specific capacitance, high reversibility, high power property, and good frequency response) between 0 and 1.0 V in 0.1 M Na$_2$SO$_4$. The specific capacitance of a-MnO$_x \cdot n$H$_2$O was as high as *ca.* 230 F g^{-1} and was found to strongly depend on the deposition modes, resulting from differences in the nanostructures. The capacitive performance of all deposits plated with different modes was very similar (with the exception of specific capacitance) because these deposits showed a very similar oxidation state with a nonstoichiometric nature, demonstrated by XPS spectra.

Acknowledgments

References

1. B. E. Conway, *Electrochemical Supercapacitors*, Kluwer-Plenum Publishing Co., New York, p. 29 (1999).
2. A. Burke, *J. Power Sources,* **91**, 37 (2000).
3. S. Nomoto, H. Nakata, K. Yoshioka, A. Yoshida, and H. Yoneda, *J. Power Sources,* **97-98**, 807 (2001).
4. L. P. Jarvis, T. B. Atwater, and P. J. Cygan, *J. Power Sources,* **79**, 60 (1999).
5. T.-C. Weng and H. Teng, *J. Electrochem. Soc.,* **148**, A368 (2001).
6. J. P. Zheng, P.-J. Cygon, and T. R. Jow, *J. Electrochem. Soc.,* **142**, 2699 (1995).
7. C.-C. Hu and Y.-H. Huang, *J. Electrochem. Soc.,* **146**, 2465 (1999).
8. C. Lin, J. A. Ritter, and B. N. Popov, *J. Electrochem. Soc.,* **145**, 4097 (1998).
9. M. Endo, T. Maeda, T. Takeda, Y. J. Kim, K. Koshiba, H. Hara, and M. S. Dresselhaus, *J. Electrochem. Soc.,* **148**, A910 (2001).
10. C.-C. Hu and K.-H. Chang, *Electrochim. Acta,* **45**, 2685 (2000).
11. C.-C. Hu and C.-Y. Cheng, *Electrochem. Solid-State Lett.,* **5**, A43 (2002).
12. C.-C. Hu and C.-H. Chu, *J. Electroanal. Chem.,* **503**, 105 (2001).
13. S.-C. Pang, M. A. Anderson, and T. W. Chapman, *J. Electrochem. Soc.,* **147**, 444 (2000).
14. H. Y. Lee, S. W. Kim, and H. Y. Lee, *Electrochem. Solid-State Lett.,* **4**, A19 (2001).
15. J. Jiang and A. Kucernak, *Electrochim. Acta,* **47**, 2381 (2002).
16. M. M. Doeff, A. Anapolsky, L. Edman, T. J. Richardson, and L. C. De Jonghe, *J. Electrochem. Soc.,* **148**, A230 (2001).
17. C.-C. Hu and T.-W. Tsou, *Electrochem. Commun.,* **4**, 105 (2002).
18. C.-C. Hu and T.-W. Tsou, *Electrochim. Acta,* **47**, 3523 (2002).
19. *Handbook of X-Ray Photoelectron Spectroscopy*, C. D. Wagner, W. M. Riggs, L. E. Davis, J. F. Moulder, and G. E. Muilenberg, Editors, p. 74, Perkin-Elmer, Eden Prairie, MN (1979).
20. M. Chigane and M. Ishikawa, *J. Electrochem. Soc.,* **147**, 2246 (2000).
21. M. Chigane, M. Ishikawa, and M. Izaki, *J. Electrochem. Soc.,* **148**, D96 (2001).
22. P. Rasiyah and A. C. C. Tseung, *J. Electrochem. Soc.,* **131**, 803 (1984).
23. A. J. Bard and L. R. Faulkner, *Electrochemical Methods, Fundamentals and Applications*, p. 14, John Wiley & Sons, Singapore (1980).
24. C. Niu, E. K. Sichel, R. Hoch, D. Moy, and H. Tennent, *Appl. Phys. Lett.,* **70**, 1480 (1997).
25. K. Jurewicz, S. Delpeux, V. Bertagna, F. Beguin, and E. Frackowiak, *Chem. Phys. Lett.,* **347**, 36 (2001).